ADVANCED OPTICAL MATERIALS
www.advopticalmat.de

# Realization of Tunable Topological Index-Near-Zero Modes in Chern Photonic Crystals

*Jie Xu,* Yamei Luo, Mengting Yang, Yun Shen, Yun You,* Kosmas L. Tsakmakidis,* and Qian Shen**

**The index-near-zero (INZ) mode exhibits novel spatial phase invariance characteristics. Recent research has focused on exploring INZ-related phenomena using metamaterials, metasurfaces, and photonic crystal (PhC) structures. However, most currently proposed INZ modes lack flexible control and are challenging to implement. Additionally, INZ modes near the Dirac point in PhCs typically operate only at specific frequencies. In this study, Chern PhCs composed of simple magneto-optical materials are utilized to regulate topologically unidirectional INZ electromagnetic modes by adjusting the air thickness and varying the magnitude of an external magnetic field. Due to the unidirectional robustness and near-zero phase shift characteristics of the INZ mode, three application scenarios are proposed: a phase inverter, a perfect 50/50 splitter, and high-performance broadband sensors. This work provides a new platform and approach for optical communication and computing.**

## 1. Introduction

In classical physics, reciprocity has always been an intuitive and fundamental property. For example, according to the principle of reversibility of light paths, changing the position of a light source allows light to travel back and forth along the same path. However, it wasn't until 1980, when K. v. Klitzing et.al. discovered the existence of topologically protected chiral edge states in the integer quantum Hall effect,[1] that the important property of non-reciprocity gained significant attention. Non-reciprocity, where light or electromagnetic (EM) waves exhibit different transmission characteristics in opposite directions, is undoubtedly a crucial feature. This property can be exploited to realize slow light,[2,3] electromagnetic trapping,[4,5] and various optical devices, such as all-optical computing.[6–8] Similar to the topological states of electrons in the quantum Hall effect, in 2008, Z. Wang et al., demonstrated the realization of topologically protected chiral edge states in the microwave regime by constructing photonic crystals (PhCs) with ferromagnetic materials,[9] and successfully build such a device one year later.[10] Since then, the so-called 'topological photonics/insulator' emerges as a new branch of optics.

Chern insulator/PhCs is one of the most important kinds of topological PhCs, and it is characterized by broken time-reversal symmetry and Chern number.[11,12] From a physical perspective, the number and propagation direction of the edge states in Chern PhCs are related to the Chern number—which is known as the bulk-edge correspondence.[13,14] Utilizing magnetized gyromagnetic materials such as yttrium iron garnet (YIG) is not only a simple but also is an efficient way to build Chern PhCs in microwave regime. In the last decades, amount of 2D were theoretically proposed and experimentally designed. Besides, fractional Chern insulator,[15,16] valley Chern PhCs,[17–19] and acoustic Chern PhCs[20] were also widely studied in rencent years. In 2022, G. Liu et al. successfully designed and achieved the first 3D Chern PhC in experiment,[21] which showcases a promissing route to light/wave manipulation and optical communication.

Artificial metamaterials provide an alternative means to control EM waves.[22–25] Negative and near-zero refractive index ($n = \sqrt{\varepsilon\mu}$) metamaterials enable key functions such as perfect lenses[26,27] and significant field enhancement.[28] Specifically, an index-near-zero (INZ) metamaterial acts as a 'spatio-temporal tunnel' for waves, allowing them to pass through without phase shift, making the output wave theoretically identical to the input. Owing to their ability to enhance optical nonlinearities, INZ modes and metamaterials have attracted growing interest in

J. Xu, Y. Luo, M. Yang
School of Medical Information and Engineering
Southwest Medical University
Luzhou 646000, China
E-mail: xujie@swmu.edu.cn
Y. Shen
Institute of Space Science and Technology
Nanchang University
Nanchang 330031, China
Y. You
School of Science
East China JiaoTong University
Nanchang 330013, China
E-mail: 3494@ecjtu.edu.cn
K. L. Tsakmakidis
Section of Condensed Matter Physics
Department of Physics
National and Kapodistrian University of Athens, Panepistimioupolis
Athens GR-157 84, Greece
E-mail: ktsakmakidis@phys.uoa.gr
Q. Shen
School of Electronic Information Engineering
China West Normal University
Nanchong 637009, China
E-mail: qianshen913@cwnu.edu.cn

The ORCID identification number(s) for the author(s) of this article can be found under https://doi.org/10.1002/adom.202501115

**DOI: 10.1002/adom.202501115**

 

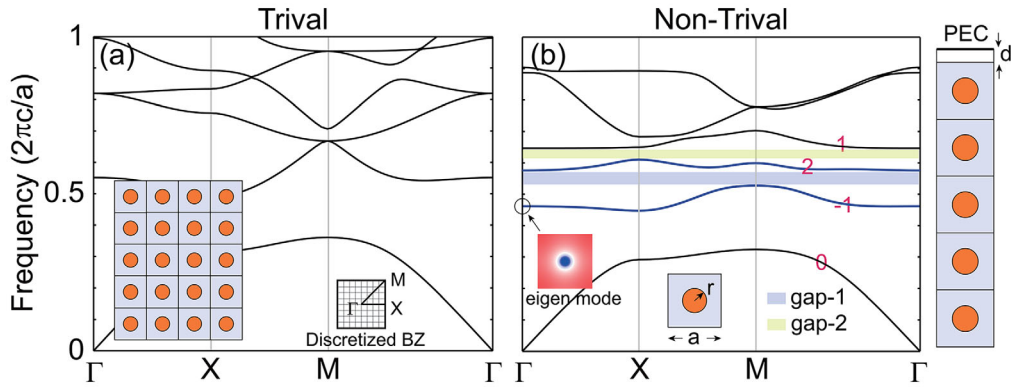


**Figure 1.** Band diagrams of YIG-based photonic crystals (PhCs). a) Trivial bands of PhCs composed of unmagnetized YIG and b) non-trivial bands of PhCs composed of magnetized YIG (highlighted by orange circles). The cyan and yellow shaded regions represent the topological one-way bands. The variable $d$ denotes the thickness of the air layer covering the structure. For magnetized YIG, the parameters are $B_0 = 1500$ G and $f_0 = 4$ GHz, inducing $\mu_1 \approx 13.764$ and $\mu_2 \approx 12.156$. Note that the permittivity of YIG is set to be 15 in this paper. The radius is $r = 0.11a$, where $a$ is the lattice constant of the PhC, as shown in the inset of (a).

nonlinear optics.[29,30] Recently, Bi et al. reported a markedly enhanced nonlinear response using quasi-bound states in the continuum with near-zero index.[31] Such metamaterials can also be realized using PhCs. For instance, PhCs with Dirac-cone bands can support equivalent INZ modes near the Dirac point.[32–34] Unlike the traditional epsilon-near-zero (ENZ, with $\epsilon \approx 0$) mode, the INZ mode in these PhCs retains an invariant spatial phase ($k = 0$) but with a finite group velocity ($v_g \neq 0$).[35,36] However, the INZ mode in current PhCs is limited by discontinuous working frequencies, rigid manufacturing processes, and limited tunability due to the required energy band structures.[37] In this work, we employ magnetized YIG to design a simple 2D Chern PhC. By tuning the parameters, nontrivial PhC bandgaps with nonzero gap Chern number ($C_g$)[38] can be achieved. According to the bulk-edge correspondence, a waveguide constructed by coupling this PhC with air and metal (PEC) can support topological one-way edge modes. The thickness of the air layer and the external magnetic field (EMF) can be adjusted to control these modes. Frequency-domain and time-domain simulations will demonstrate that the broadband and tunable INZ modes are robust against sharp corners, obstacles, and material losses. Based on the tunable topological INZ modes, we propose three optical devices: a phase inverter, a 50/50 splitter, and two broadband topological sensors. The proposed INZ modes in Chern PhCs extend existing INZ systems and are applicable in optical communication.

## 2. Results

### 2.1. Truly INZ Modes in Photonic Crystals

Initially, we consider a 2D PhC, as depicted in the inset of **Figure** 1a. The PhC consists of YIG rods (indicated by orange circles) surrounded by air (gray regions). As shown in Figure 1a, no topological band exists when the YIG rods are unmagnetized ($\mu_r = \mu_0$), and all bulk bands are trivial, which is expected since time-reversal symmetry remains unbroken. Conversely, applying a uniform EMF ($B_0$) induces magnetization in the YIG rods through the magneto-optical effect, thereby breaking time-reversal symmetry. Here, we apply an EMF in the -z direction with $B_0 = 1500$ G to the structure, and the relative permeability tensor of the YIG rods is expressed as follows:

$$\bar{\mu} = \begin{bmatrix} \mu_1 & -i\mu_2 & 0 \\ i\mu_2 & \mu_1 & 0 \\ 0 & 0 & 1 \end{bmatrix} \tag{1}$$

where $\mu_2 \neq 0$ and the off-diagonal ratio is also nonzero, inducing the nonreciprocal propagation of a TE wave. It is effective to determine whether a topological bandgap has been engineered by plotting the PhC band diagram and calculating the Chern numbers of each band for specific values of $\mu_1$ and $\mu_2$.[9] In Figure 1b, we set the frequency ($f_0$) in YIG to 4 GHz, with $\mu_1 \approx 13.764$ and $\mu_2 \approx 12.156$. As a result, Figure 1b shows that the connections between the second and third, and third and fourth bulk bands are untied at the 'M' and 'Γ' points, respectively. Two bandgaps (gap-1 and gap-2) are clearly formed upon the application of the EMF. Specifically, gap-1 and gap-2 correspond to the frequency ranges $0.527\ c/a < f < 0.576\ c/a$ and $0.611\ c/a < f < 0.647\ c/a$, respectively. One-way modes may occur in these band gaps due to $T$ symmetry breaking, with the critical criterion for evaluation being the Chern number, defined as follows,[9,39]

$$\begin{aligned} C_n &= \frac{1}{2\pi i}\int_{BZ} d^2k\left(\frac{\partial \mathcal{A}_y^{nn}}{\partial k_x} - \frac{\partial \mathcal{A}_x^{nn}}{\partial k_y}\right) \\ \vec{\mathcal{A}}^{nn'}(k) &\equiv \langle E_{nk}|\nabla_k|E_{n'k}\rangle \end{aligned} \tag{2}$$

for the $n$th band. In our proposed structure, the Chern number of each band can be calculated[40] by: 1) discretizing the Brillouin zone (BZ), as shown in the inset of Figure 1a; 2) calculating the eigenmodes for each $[k_x, k_y]$ in the BZ (see the inset of Figure 1b) using the finite-element method (FEM) in the COMSOL Multiphysics software; and 3) determining the Berry connection and Chern number using Equation (2). According to our calculations, the gap Chern numbers ($C_g$) of the two bandgaps are -1 (gap-1) and +1 (gap-2), which implies the expectation of two oppositely propagating, topologically protected edge modes in gap-1 and gap-2 when an air layer is placed on the PhC, as shown in

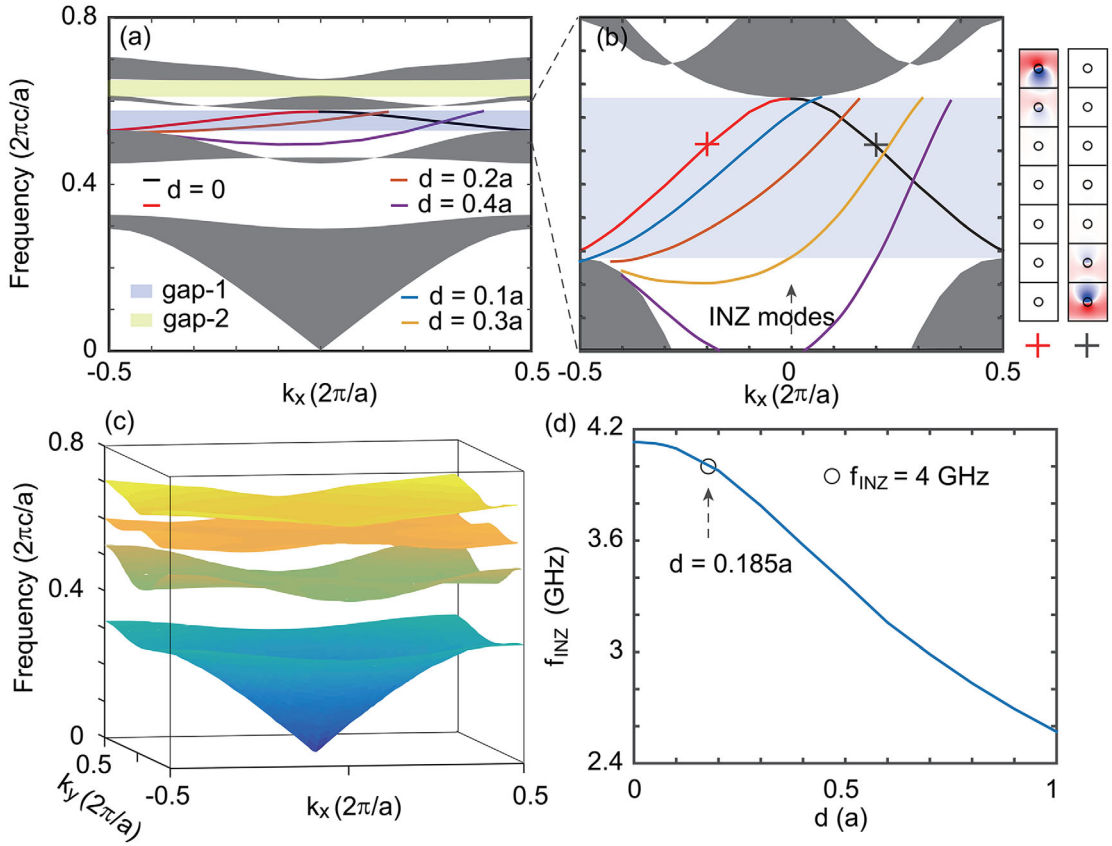


**Figure 2.** The relationship between the parameter $d$ and the INZ mode frequency $f_{INZ}$. a, b) Dispersion curves of the edge states for $d = 0$ (red and black lines), $d = 0.1a$ (blue line), $d = 0.2a$ (brown line), $d = 0.3a$ (yellow line), and $d = 0.4a$ (purple line). The rightmost panel shows the electric field distributions of the eigenmodes (indicated by the red and black crosses in panel (b)) for the PhC structure with $d = 0$ (i.e., without the cladding air layer), evaluated at $|k_x| = 0.4\pi/a$. In the YIG region, the material parameters are set as $f = f_0 = 4$ GHz, $\mu_1 \approx 13.764$, and $\mu_2 \approx 12.156$. c) The complete bulk band of the PhC with magnetized YIG. Note that the gray-shaded regions in (a) and (b) represent the corresponding projected bulk dispersion. (d) $f_{INZ}$ as a function of $d$ at $f_0 = 4\sim$GHz. Here, $a = 0.0418\sim$m, and all other parameters match those in Figure 1.

the right panel of Figure 1b. It is worth noting that, theoretically, it is essential to place another trivial PhC with overlapping gap-1 and gap-2 on our designed structure to sustain topological modes. However, in this paper, we set a simple PEC wall to terminate the air layer, which has been widely proven to be an efficient method for engineering a 'pathway' for topological edge modes. This approach is also demonstrated to be suitable for tuning the topological INZ modes discussed below.

For gap-1, we first calculated the dispersion curves for various $d$ values, the thickness of the cladding air. As shown in Figure 2a,b, clear one-way propagation modes are observed, except for $d = 0$, where the symmetric bands (marked by red and black lines) propagate on the top and bottom PEC walls, as seen in the right panel of Figure 2b. Additionally, the dispersion curves of the edge modes decrease in gap-1 as $d$ increases, or equivalently, as the PEC is shifted upward. As emphasized in Figure 2b, several INZ modes with $k = 0$ emerge in gap-1 as $d$ changes from 0 to $0.4a$. A more complex bulk band diagram in the BZ of the PhC is shown in Figure 2, with gap-1 around $f = 0.55c/a$ and gap-2 around $f = 0.63c/a$. In our previous analysis, we assumed a constant frequency of 4 GHz in YIG, which is technically correct for calculating or estimating the bandgap around $f = f_0 = 4$ GHz, but not theoretically accurate. Theoretical calculation of the edge mode dispersion in gap-1 is also challenging. However, focusing only on the INZ modes simplifies the analysis. As shown in Figure 2d, we fix $k = 0$ [in contrast to the full range $-\pi/a < k < \pi/a$ in Figure 2a] and set $a = 0.0418$ m to compute the INZ eigenfrequencies as a function of $d$ using COMSOL. The resulting INZ frequency $f_{INZ}$ is plotted versus $d$, where the initial guess $f_0 = 4$ GHz $\approx 0.558c/a$. A similar decreasing trend was observed as $d$ increased from near zero to $d = a$. Notably, an INZ mode with frequency $f = f_{INZ} = f_0 = 4$ GHz emerges at $d \approx 0.185a$; unlike other modes along the fitting curve in Figure 2d, this mode qualifies as a truly INZ mode, as its frequency exactly matches the preset value $f_0$, whereas other modes exhibit a nonzero wavenumber ($k \neq 0$) due to deviations from $f_0$. It is worth noting that the proposed INZ modes in other works using techniques like effective medium theory are theoretically feasible but remain technically challenging. In contrast, the INZ modes in Chern PhCs proposed here are more promising for practical use, as the value of $d$ can be easily optimized to excite and sustain the INZ modes.

By continuously varying the preset frequency $f_0$ and computing the corresponding eigenfrequencies at $k = 0$ for different values of $d$, additional truly INZ modes satisfying $f_{INZ} = f_0$ can be identified. To accurately determine each INZ frequency, we apply an iterative method: starting from $f = f_0 = 4$ GHz, we extract the

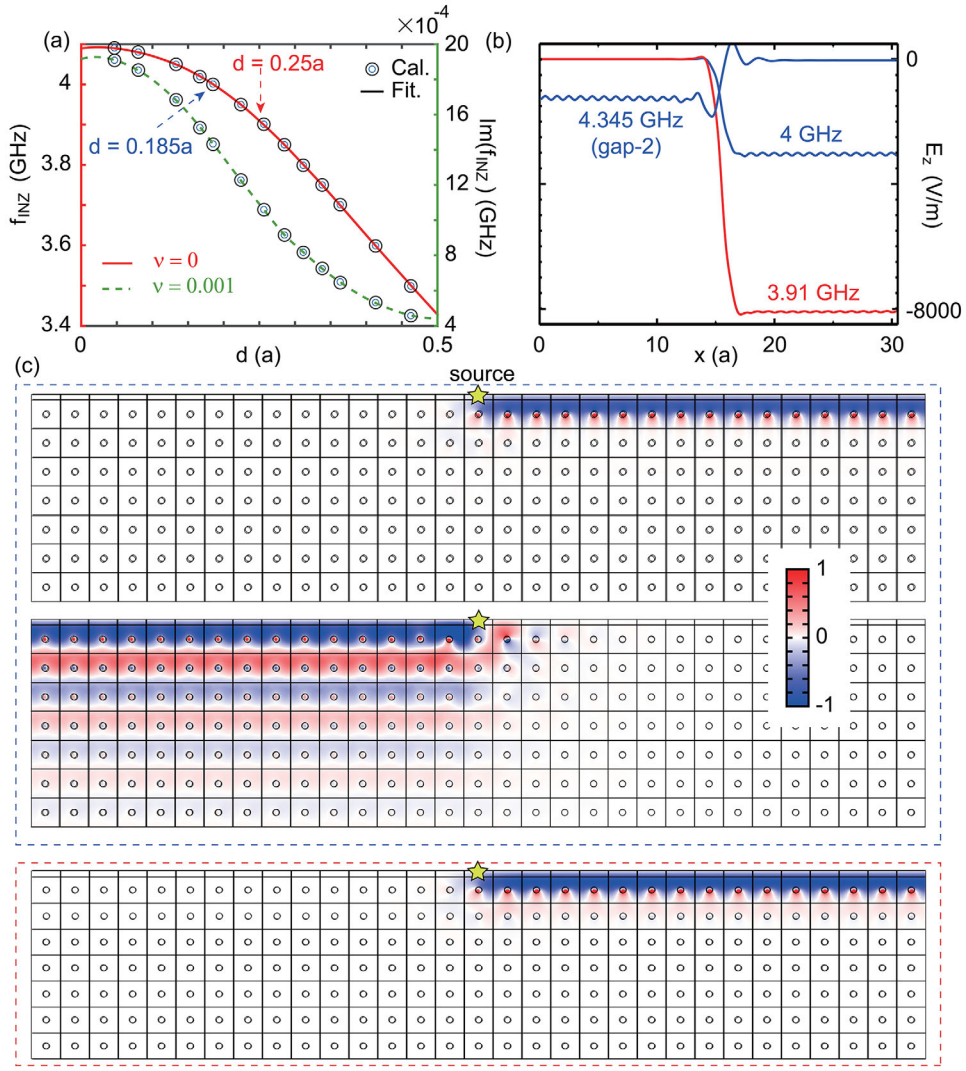


**Figure 3.** Truly tunable and topologically protected one-way INZ modes in Chern PhCs. a) $f_{INZ}$ (solid line) and the imaginary part of the frequency (Im($f_{INZ}$), dashed line) are plotted as functions of $d$ at $f = f_0$. A damping parameter $\nu = 0.001$ was used to study the loss effect on the INZ modes with complex frequencies. b, c) Electric field distributions (b) along the air—PhC interface and (c) in the system from FEM simulations with $\nu = 0.001$. The blue and red lines/regions correspond to $d = 0.185a$ and $d = 0.25a$, respectively. The operating frequencies of the simulations in (c) are $f = 4$ GHz ($\mu_1 \approx 13.764$ and $\mu_2 \approx 12.156$), $f = 4.345$ GHz ($\mu_1 \approx -15.895$ and $\mu_2 \approx -17.478$), and $f = 3.91$ GHz ($\mu_1 \approx -9.9$ and $\mu_2 \approx -8.286$) from top to bottom. The middle panel of (c) presents a FEM simulation of INZ modes in gap-2. $r = 0.11a$ and $a = 0.0418$ m.

simulated eigenfrequency $f_1$, then update the preset as $f = f_0 = (4 + f_1)/2$ GHz. This process is repeated until the input and output frequencies converge. As shown in **Figure 3a**, the converged INZ frequencies for various $d$ values are marked by circles, and the red curve represents a fit to the calculated data. Moreover, to evaluate the effect of material loss on the INZ modes, a typical damping parameter $\nu = 0.001$ for high-quality YIG[21,41,42] is considered in Figure 3a. Our simulations show that the real part of the INZ frequency, Re($f_{INZ}$), remains nearly unchanged for all identified INZ modes, while only a very small imaginary (Im($f_{INZ}$)) component appears. These results indicate that the proposed INZ modes in PhCs are robust against material damping. It is quite clear that tunable and broadband INZ modes exist with 3.4GHz $< f_{INZ} <$ 4.2GHz when $d$ changes from near zero to $0.5a$. The Chern number associated with gap-1 is $-1$. According to the bulk—edge correspondence, this guarantees the existence of a forward-propagating ($v_g > 0$) edge state at the air—PhC interface. Since edge states are topologically protected against backscattering, the combination of cladding metal/PEC, PhC, and surrounding air effectively forms a 'one-way resonator'. Numerical simulations further confirm that the field profiles of the eigenmodes remain nearly unchanged across the Brillouin zone when $d$ takes specific values. As $d$ increases, the eigenfrequencies—including those of the INZ modes—redshift (e.g., $f_{INZ}$ decreases, as shown in Figure 3a), consistent with the behavior of Fabry—Pérot (FP) resonators and dielectric waveguides. This indicates that the INZ modes can be effectively tuned by varying $d$.

Two cases, $d = 0.185a$ and $d = 0.25a$, were chosen to verify this decreasing relationship, and as shown in Figure 3a, the

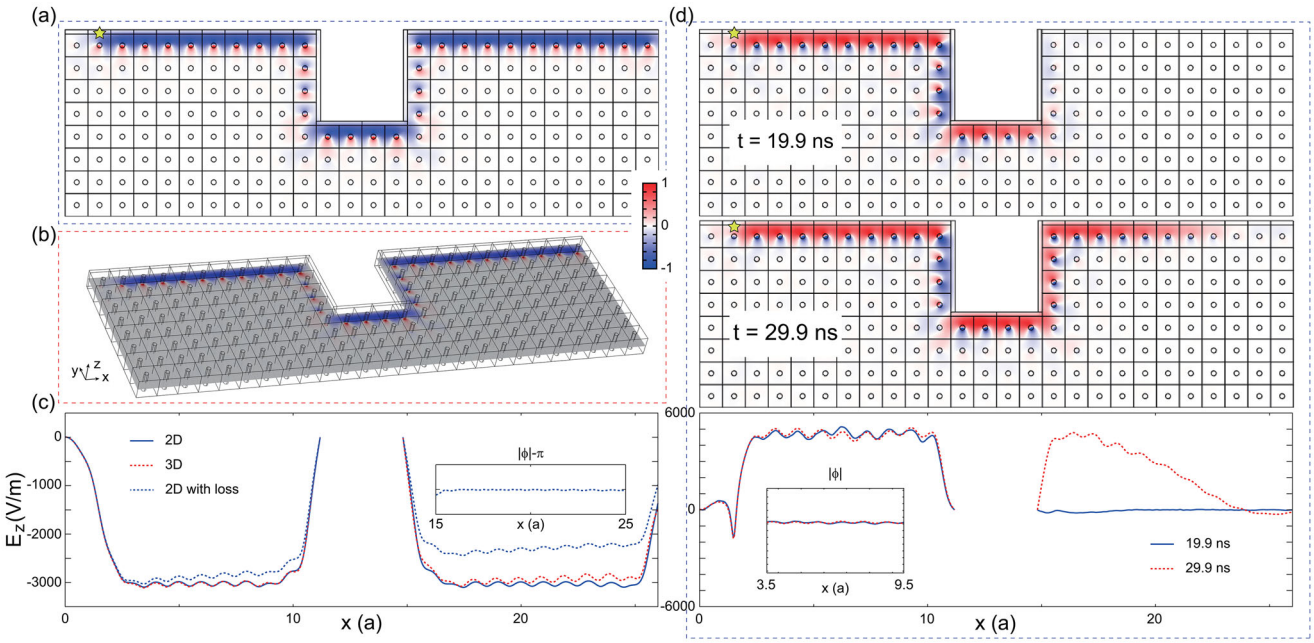


**Figure 4.** Topological one-way INZ modes in 3D and their simulation in the time domain. Simulation results for a) 2D and b) 3D topological INZ modes. c) Electric field distributions along the center of the air layer in lossless 2D and 3D FEM simulations, and in the 2D case with $\nu = 0.001$. The inset shows the electric-field phase ($\phi$) in the final part with the loss effect included. d) Simulation of one-way INZ modes in the time domain. $f = f_0 = 4$ GHz ($\mu_1 \approx 13.764$ and $\mu_2 \approx 12.156$), $d = 0.185a$, $r = 0.11a$, and $a = 0.0418$ m.

corresponding INZ frequencies are 4 and 3.91 GHz, respectively. The simulation results are shown in Figure 3b,c. We emphasize that in all FEM simulations, a line current source was employed to excite the one-way edge modes, with PEC boundaries applied on both sides. The electric field ($E_z$) distribution is shown in the top ($f = 4$ GHz) and bottom ($f = 3.91$ GHz) panels of Figure 3c. It can be seen that the excited waves propagate unidirectionally along the air-PhC interface in both cases, with near-zero phase shift during propagation. Clearer results are depicted in Figure 3b, where the blue and red lines represent the $E_z$ distribution of the edge modes in the simulations (as shown in Figure 3c). Similarly, $E_z$ exhibits no variation between different units. Another blue line and the middle panel in Figure 3c represent the $E_z$ distribution of a higher-order INZ mode in gap-2 with $d = 0.185a$ and $f_{\mathrm{INZ}} = f_0 = 4.345$ GHz, as predicted in previous analyses and calculated using an iterative method. We emphasize that our proposed dual-band INZ structure is highly important for INZ mode-based optical communication and computing, and it is significantly more efficient compared to other proposed INZ systems and structures in both theory and engineering due to its high tunability. We will discuss the higher-order INZ modes in the text below. We also note that Figures 2 and 3 provide an efficient method to engineer suitable edges/structures supporting truly INZ modes. First, a Chern PhC should be designed so that the frequency $f_0$ resides within a non-trivial bandgap ($C_g \neq 0$). Subsequently, the parameter $d$ can be readily adjusted and computed to determine the eigenfrequency of the INZ modes using FEM.

One of the most important advantages of topological one-way modes in Chern PhCs is their robustness to imperfections or disorders in the system. As shown in **Figure** 4a, we designed a large rectangular hole ($4a \times 4a$) in the passing channel route for the one-way INZ modes. In the 2D condition, as shown in Figure 4a, the INZ wave propagates unidirectionally toward the rectangle and completely bypasses it with nearly no phase shift. In Figure 4b, a 3D simulation was performed to further illustrate the robustness of the INZ modes in PhCs for a more realistic case. Similar to the 2D case, the wave was successfully excited and propagated in only one direction, and the electric field remained unchanged after propagating a length of $L = 20a$. Figure 4c shows the electric field distribution of the INZ modes along the air-PhC interface, and it can be seen that the wave remains almost unchanged in the first and third regions (the excited and output regions) in both 2D and 3D cases. The slight differences between the 2D and 3D simulations near the end face can be attributed to the coarser mesh resolution in the 3D simulation. This numerical artifact becomes more pronounced with increasing propagation distance, while the initial propagation region shows better agreement between the 2D and 3D results, consistent with theoretical expectations. To eliminate the impact of loss on topological one-way INZ modes, we set a damping parameter of $\nu = 0.001$ in the 2D case. As shown by the blue dashed line in Figure 4c, the electric field gradually decreases during propagation. However, as shown in the inset of Figure 4c, the output electric-field phase remains unchanged in the final region of the structure. Therefore, it is important to note that our proposed truly topological one-way INZ modes are also robust to material loss, further enhancing the application of INZ modes in phase-based optical devices.

The existence of truly INZ modes is also verified in the time domain. As shown in Figure 4d, a line current source ($I = exp(i2\pi f_0 t)$) was used to excite the INZ modes. The first two

 

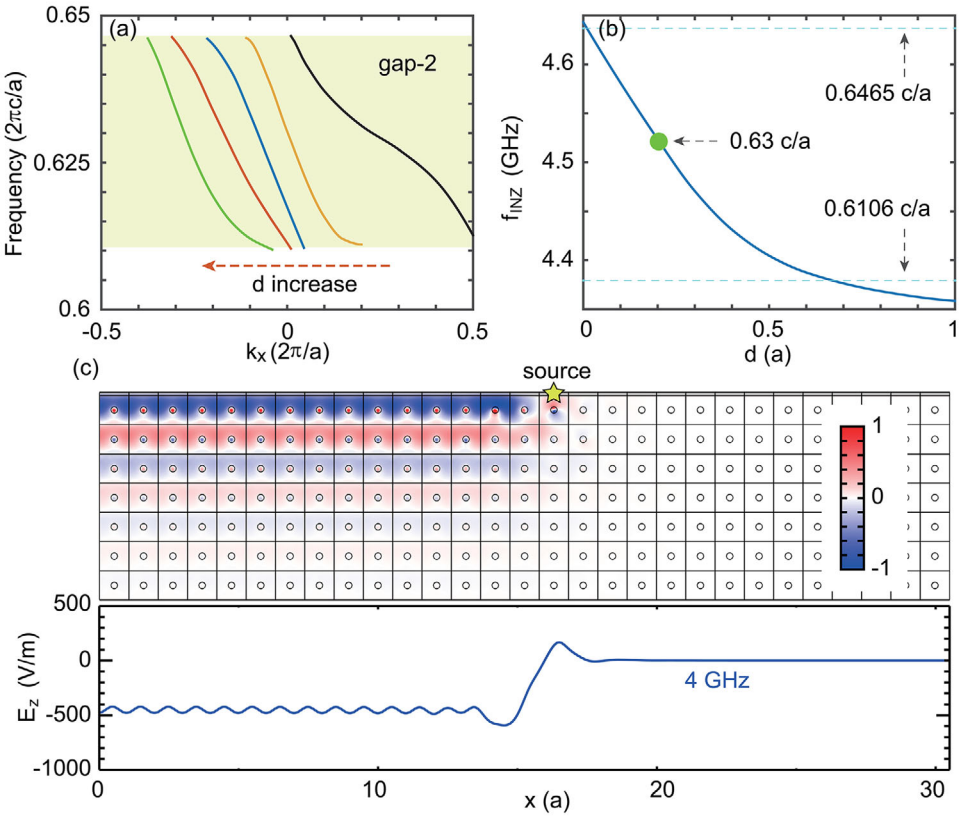


**Figure 5.** INZ modes in the higher-order one-way band. a) Dispersion curves of edge modes in gap-2 for $d = 0$ (black), $d = 0.1a$ (yellow), $d = 0.2a$ (blue), $d = 0.3a$ (red), and $d = 0.4a$ (green), with $f_0 = 4$ GHz. b) Relationship between $d$ and $f_{INZ}$ in gap-2 as $a = 0.0418$ m. Horizontal lines indicate the gap-2 band limits. c) Upper panel: Simulation results for one-way INZ modes in gap-2. Lower panel: Electric field distribution of the INZ modes along the center of the air layer in the upper panel. Here, $f = f_0 = f_{INZ} = 0.63a = 4$ GHz (green point in (b)), $\mu_1 \approx 13.764$, $\mu_2 \approx 12.156$, and $d = 0.104a$ ($a = 0.0472$ m).

images demonstrate that a one-way EM wave was excited and, consistent with the FEM simulations in the frequency domain, it can bypass the large corner with no backscattering. Moreover, the electric field appears the same along the air-PhC interfaces, as seen in the first two regions. The third image further confirms that the wave has near-zero wavenumber since the phase shift is nearly zero (see the inset) after a $\Delta t = 10$ ns ($=40T_0$, $T_0 = 1/f_0 = 0.25$ ns) of propagation. Note that the nonuniform $E_z$ in the third region is due to the limited time evolution and the time step constraints of our computational resources. The frequency-domain and time-domain simulations demonstrate the robustness of topological one-way INZ modes at the edge of the proposed Chern PhCs. These modes propagate with near-zero spatial phase shift and are affected *only* by time-dependent oscillations ($\phi_{out} = \phi_{in} \pm \omega t$)).

We have previously studied the topological INZ modes in the gap-1 region of the PhC, demonstrating their robustness to large corners and tunability via air layer thickness over a wide band. We now discuss the higher-order topological INZ modes in the gap-2 region. **Figure** 5a shows the dispersion diagram of the edge modes in gap-2 for five different $d$, with $f_0 = 4$ GHz and $r = 0.11a$. Since $C_g = +1$ for gap-2, only one dispersion curve with a negative slope (i.e., backward propagating) appears in each case. As $d$ increases, the curves shift downward, indicating a decrease in $f_{INZ}$. Assuming $a = 0.0418$ m, as in Figure 2, $f_{INZ}$ (shown in Figure 5b) is permanently larger than $f_0$ (=4 GHz) in gap-2, constrained between $0.6106c/a$ and $0.6465c/a$. In summary, these 'INZ' modes are not physical due to the inconsistency between $f_0$ and $f_{INZ}$. A simple solution is to optimize parameter $a$ to place $f_0$ within the gap-2 region. For example, setting $a = 0.0472$ m places $f_0$ ($\approx 0.63c/a$) near the center of the bandgap, with $d = 0.104a$ according to our calculations. The simulation result for the revised PhC, shown in Figure 5c, reveals a backward propagating INZ mode.

Similar to the INZ modes in gap-1, the INZ modes in gap-2 can also be tuned by varying $d$. Furthermore, owing to the magneto-optical effect of the YIG rods, our proposed truly INZ modes can be readily controlled by adjusting the EMF ($B_0$). Using FEM, we calculated the eigen modes at $k = 0$ for a PhC with parameters $r = 0.11a$, $d = 0.104a$, and $a = 0.0472$ m, as shown in the solid line in **Figure** 6a. For $B_0 = 1500$ G, we obtained $f_{INZ} \approx 4$ GHz, consistent with the results presented in Figure 5. As the EMF increases, $f_{INZ}$ exhibits a gradual increase within the range $1000\,\text{G} < B_0 < 2000\,\text{G}$. Notably, the rate of change in $f_{INZ}$ is more pronounced in the region $1000\,\text{G} < B_0 < 1500\,\text{G}$ compared to $B_0 > 1500$ G, indicating that INZ modes are more sensitive to tuning under relatively small EMF. The loss effect was also evaluated for varying values of $B_0$. Similar to the results in Figure 3a, the real

 

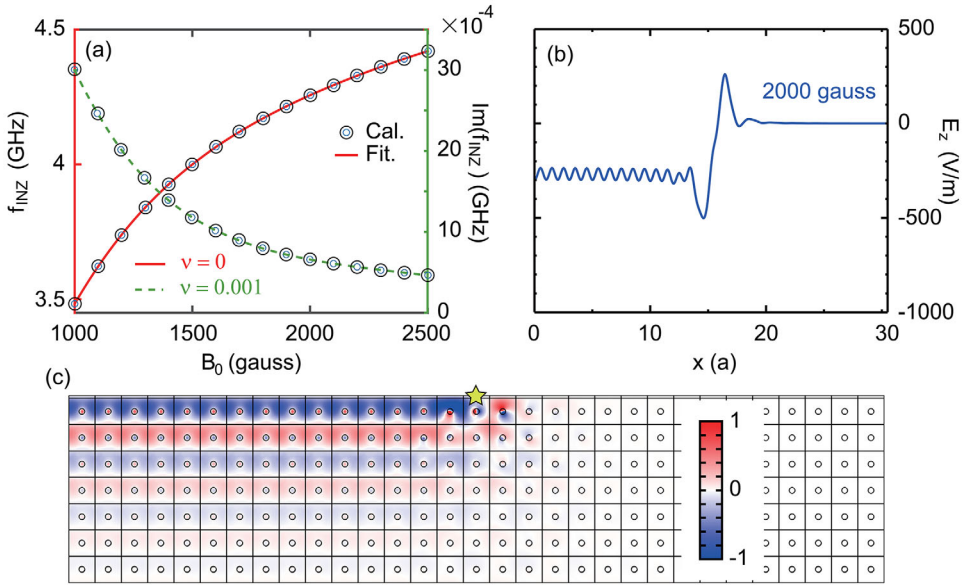


**Figure 6.** Tunable topological one-way INZ modes in gap-2 by varying the external magnetic field (EMF). a) $f_{INZ}$ (solid line) and Im($f_{INZ}$) (dashed line) as functions of the EMF. The damping parameter is set to $\nu = 0.001$ in the loss case. (b, c) Electric field distributions from FEM simulations at $B_0 = 2000$ G and the corresponding frequency $f = f_0 = f_{INZ} = 4.260$ GHz ($\mu_1 \approx 3.112$ and $\mu_2 \approx 1.607$). Other parameters: $a = 0.0472$ m, $r = 0.11a$, and $d = 0.104a$.

part of the INZ frequency, Re($f_{INZ}$), remains nearly unchanged, while a small imaginary part, Im($f_{INZ}$), appears for all INZ modes. See Figure 6a for details. To validate our calculations, we examined a case with $B_0 = 2000$ G using the same PhC configuration as in Figure 5c. The electric field distributions along the air-PhC interface (Figure 6b) and within the PhC (Figure 6c) further corroborate our theoretical predictions and calculations, demonstrating that EMF can effectively modulate the INZ modes.

### 2.2. The Applications of Truly Topological INZ Modes

In the previous subsection, we thoroughly analyzed truly topological INZ modes in Chern PhCs with robust one-way propagation characteristics. We proposed two efficient methods to control these modes by optimizing the values of $d$ and/or the EMF. The next question is how to apply these modes. A straightforward application of the truly INZ modes is the design of a simple optical phase inverter. The thickness of the air layer affects the edge modes. As discussed in Figure 3, neither increasing nor decreasing $d$ results in a non-zero $k$, thus inducing a significant phase shift or even phase inversion (e.g., $0 \rightarrow \pm\pi$). We designed a one-way waveguide composed of PhCs and air layers with varying $d$, as shown in the inset of the middle panel of **Figure 7**. In the first and last sections, $d = d_0 = 0.185a$, while for the middle section, $L_1 = 5a$ and $d = d_1$ ($d_1 > d_0$) were designed to control the output phase. Four different values of $d$ were chosen to study the phase shift between the first input and third output sections. As shown in the middle panel of Figure 7, the electric field along the air-PhC interface in each cell remains nearly the same in the first and last sections, while experiencing a significant phase shift in the second, relatively thick section, since $k \neq 0$. The third panel and inset of Figure 7 demonstrate that as $d_1$ increases from $0.21a$ (blue line) to $0.24a$ (red line), $|E_z|$ decreases to 0 ($\phi_{E_z} = 0$) and then returns to the initial value ($\Delta\phi \approx \pi$), with $d_1 \approx 0.239a$. The first panel of Figure 7 shows the FEM simulation of the all-optical phase inverter at $f = f_0 = 4$ GHz, where the electric-field intensity in the middle cell of the second section is nearly zero, indicating a complete phase inversion in this structure. Note that all the INZ modes proposed here can also be inverted by designing similar structures, with the thickness of the air layer easily adjustable.

Splitting light or EM waves is a key research topic in the field. Our proposed PhC configuration supporting INZ modes can also be used to design a splitter. **Figure 8a** shows the dispersion diagram for odd (red line) and even (black line) modes in the PhC-based unit depicted in the images below. The splitter unit consists of two PhCs under inverse EMFs ($B_1 = -B_0$), with one layer of air between them. The last two images in Figure 8a show the symmetric and antisymmetric electric fields for the even and odd modes, respectively. Figure 8b shows the schematic of our designed optical splitter with four inputs/outputs. Based on the previous analysis, the one-way modes in gap-1 can be excited and supported in ports 1 and 3, while the one-way modes in gap-2 can be excited and supported in the remaining ports. Due to the strict symmetry, the split waves at different outputs should have nearly the same energy, and the output phases should either be the same or inverted. As shown in the first two images in Figure 8c, at $f = 4$ GHz, the waves excited from the source propagate unidirectionally and split into two channels. Our calculations show that the splitting ratio is very close to 50/50. It is also clear that the phases in the output channels are nearly the same for the even modes (see the first image) and inverted for the odd modes (see the second image). A similar conclusion can be drawn for higher-frequency cases, such as $f = f_0 = 4.35$ GHz, as shown in the last two images in Figure 8c. We emphasize that, as shown in the second and fourth images, the INZ modes provide stable and reliable phase inputs for the two outputs, which is crucial for phase-based optical computing. It is also

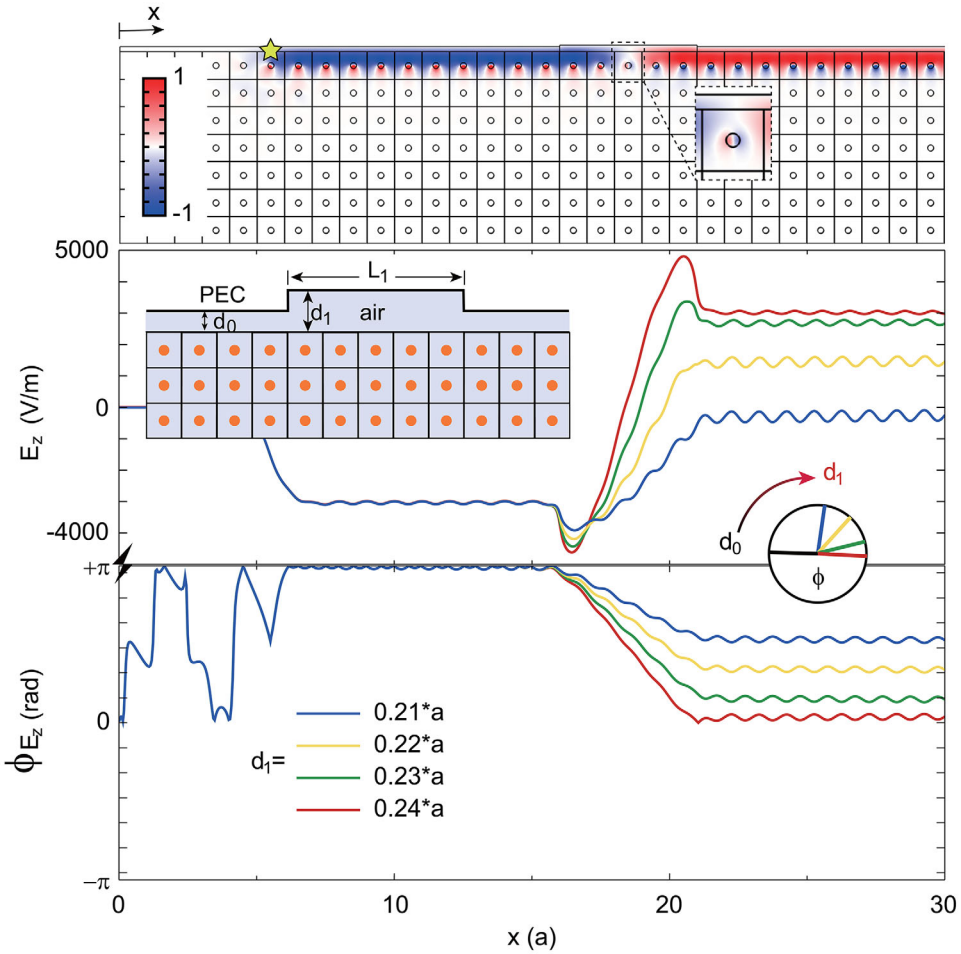


**Figure 7.** All-optical phase inverter utilizing topological INZ modes. First two panels: Electric-field distribution in the joint PhC structure, where the middle section has a thicker air layer with $d_1 = 0.239a$ (first panel, $|\Delta\phi| \approx \pi$) or $d_1 = 0.21a$ (blue line), $0.22a$ (yellow line), $0.23a$ (green line), $0.24a$ (red line), while other sections have $d_0 = 0.185a$. $L_1 = 5a$, with other PhC parameters identical to those in Figure 4. The inset shows the schematic of the all-optical phase inverter. The bottom panel shows the electric-field phase during the propagation of one-way modes.

noteworthy that the splitting ratio can be adjusted through multiple ways, such as modifying a portion of the EMFs. Based on our calculations, when the EMFs in the top-left and bottom-right regions are altered to 1400 G, the splitting ratio between the energy output from port-4 and that from port-2 is approximately 53/47.

The INZ modes studied above are robust to corners and backscattering. However, the INZ wave may be affected when it encounters imperfections or obstacles. In the ideal case, the phase of the INZ modes remains unchanged during propagation; however, in practice, the output phase may differ slightly from the input phase. Based on this phase shift, a topological detector or sensor can be designed. In this paper, we propose two types of topological sensors based on INZ modes, as shown in **Figure 9**. The schematic of the first type of sensor is shown in the inset of Figure 9a. The main structure is the same as in Figure 3, except that a rectangular ($2d \times d$, where $d$ is the thickness of the air layer) obstacle is placed at the air-PhC interface. In the simulations, the permittivity of the obstacle ($\epsilon_d$) changes from 27.65 to 35.6. As a result, the output phase gradually decreases from $+\pi$ to $-\pi$ as $\epsilon_d$ increases. For example, the left panel of Figure 9a shows the electric field in the simulations for $\epsilon_d = 29$ and $\epsilon_d = 31$, where a nearly reversed phase is observed around the output port.

The inset of Figure 9b shows the configuration of the second type of topological sensor. The input and output are traditional slab waveguides filled with air. To support modes in the [3.8GHz, 4.1GHz] range, the thickness $d_0 = 4$ cm is chosen such that the cutoff frequency $f_c \approx 3.75$ GHz. An air-PhC unit with a square ($d \times d$) obstacle is inserted into the slab waveguides. Our calculations show that the transmission of this device is relatively high over a broad band as $\epsilon_d$ changes from 36 to 48, with a red shift in the transmission peak, as shown in Figure 9b. The sensitivity of the sensor can be calculated using the formula $S = \Delta\lambda/\Delta\sqrt{\epsilon}$.[43] Based on our simulations, we found that $S \approx 7.864 \times 10^{-4}$. Note that this topological sensor facilitates back-scattering immune use of light for sensing, which is crucial for high-performance applications. The right images show that due to the differing coupling effects between the input modes (in the first part) and the edge mode (in the air-PhC unit), waves with different frequencies exhibit significantly different transmissions. It is worth noting that our proposed topological sensor has two advantages—high

 

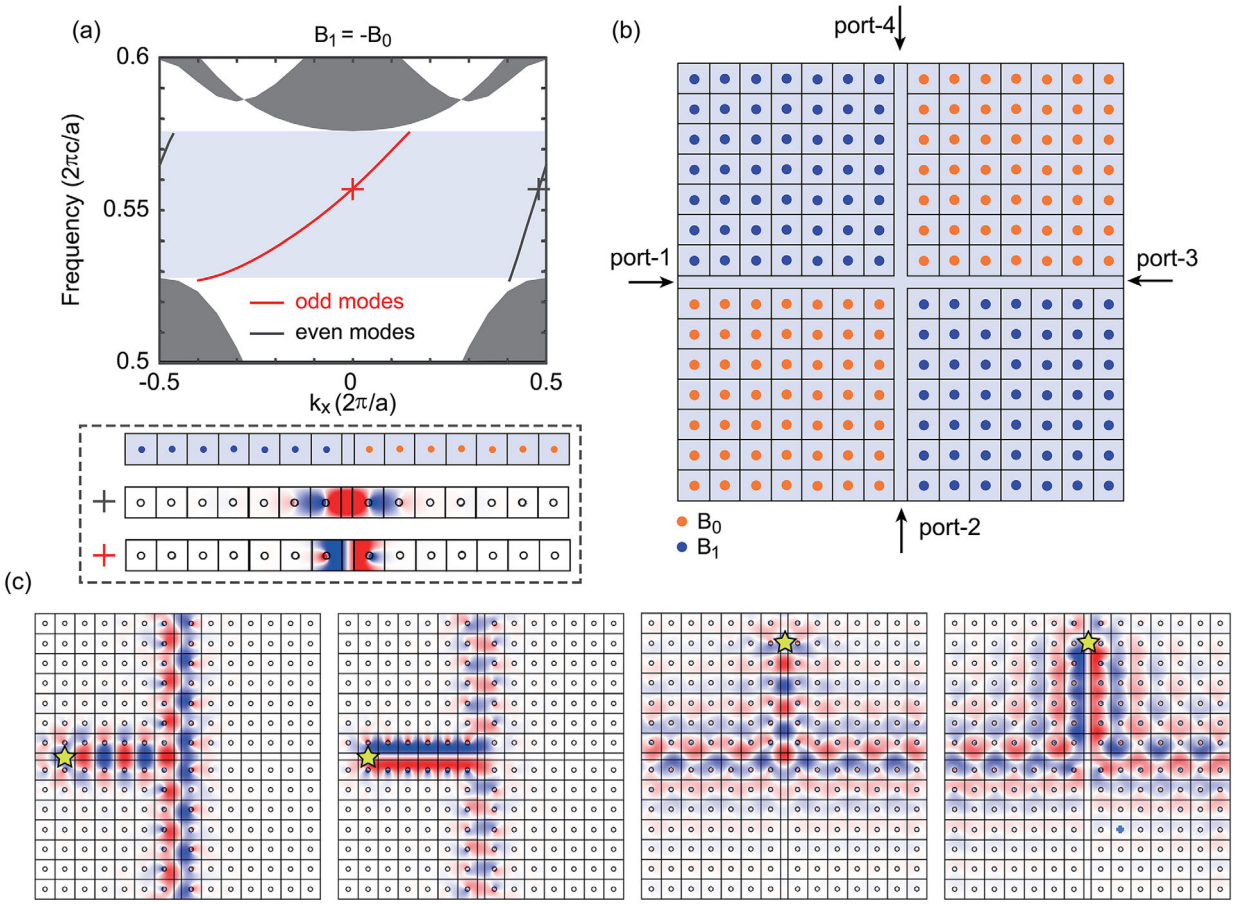


**Figure 8.** Perfect 50/50 splitters. a) Dispersion curves for odd (red line) and even (black line) modes in a PhC structure, which looks as if a square is divided into four smaller squares by a cross in the middle. Parameters: $r = 0.11a$, $a = 0.0418$ m, and $d = 0.37a$ ($=2 \times 0.185a$). Lower panel: Schematic of the splitter unit, along with the eigenmodes corresponding to the odd (indicated by red crosses) and even (indicated by red crosses) modes at $f = f_0 = 4$ GHz. b) Schematic of the cruciform structure with oppositely magnetized YIG rods (colored differently). c) Simulations conducted for both the even and odd modes, which evidently reveal that they are evenly split into two channels at $f = f_0 = 4$ GHz (as shown in the left two panels) and $f = f_0 = 4.35$ GHz (as depicted in the right two panels). For the last two panels of c), $\mu_1 \approx -15.895$ and $\mu_2 \approx -17.478$, while for the rest, $\mu_1 \approx 13.764$ and $\mu_2 \approx 12.156$.

performance and broadband—due to the topologically protected working modes, compared to other proposed sensors, such as resonant-based sensors. Our proposed tunable topological INZ modes at microwave frequencies may also be realized in other frequency regimes, such as the acoustic or optical bands, provided that the time-reversal symmetry[44,45] and/or spatial inversion symmetry[46,47] is broken in those systems.

To further demonstrate the robustness of the proposed INZ modes in Chern PhCs, the effect of material damping (i.e., $\nu$ for YIG) is examined in **Figure 10a**. For small $\nu$, the INZ mode propagates over long distances (e.g., $L = 8a$) with high transmittance, such as $T \approx 0.855$ (purple arrow in Figure 10a). As $\nu$ increases, the corresponding $T$ decreases. For large $\nu$ (e.g., $\nu = 0.01$), the INZ mode rapidly dissipates, as shown in the final panel of Figure 10a. This issue can be mitigated using advanced YIG fabrication techniques, and $\nu = 0.001$ is typical for high-quality YIG.[41] To assess the effect of structural disorder, a square silicon obstacle of side length $w = 0.5a = 0.0209$ m was introduced into the INZ system. Here, $\nu = 0.001$ is used. Figure 10b illustrates the schematic of this structure. The vertical distance between the obstacle's top edge and the top of the air layer is varied from 0 to $a$. In most cases, $T$ shows only a slight decrease compared to the case of $w = 0$ (no obstacle). Specifically, as shown in Figure 10c, the black circles (FEM-calculated $T$) remain close to the horizontal reference line, indicating the ideal case. For a smaller obstacle ($w = 0.25a = 0.01045$ m), variations in $T$ are even more negligible for different $dy$, as indicated by the red circles in Figure 10c. Notably, the INZ mode retains its one-way propagation and zero-phase-shift characteristics before and after encountering the obstacle, with only minor loss and phase shift observed near the obstacle (see inset of Figure 10c). Therefore, the proposed INZ modes are robust against typical material damping and structural disorder. High-quality YIG remains essential for optimal performance of INZ modes and related systems.

## 3. Conclusion

In this work, we propose the topologically protected one-way INZ modes with $k = 0$ in YIG-based PhCs in the microwave regime. We calculate the band structures and Chern numbers of the

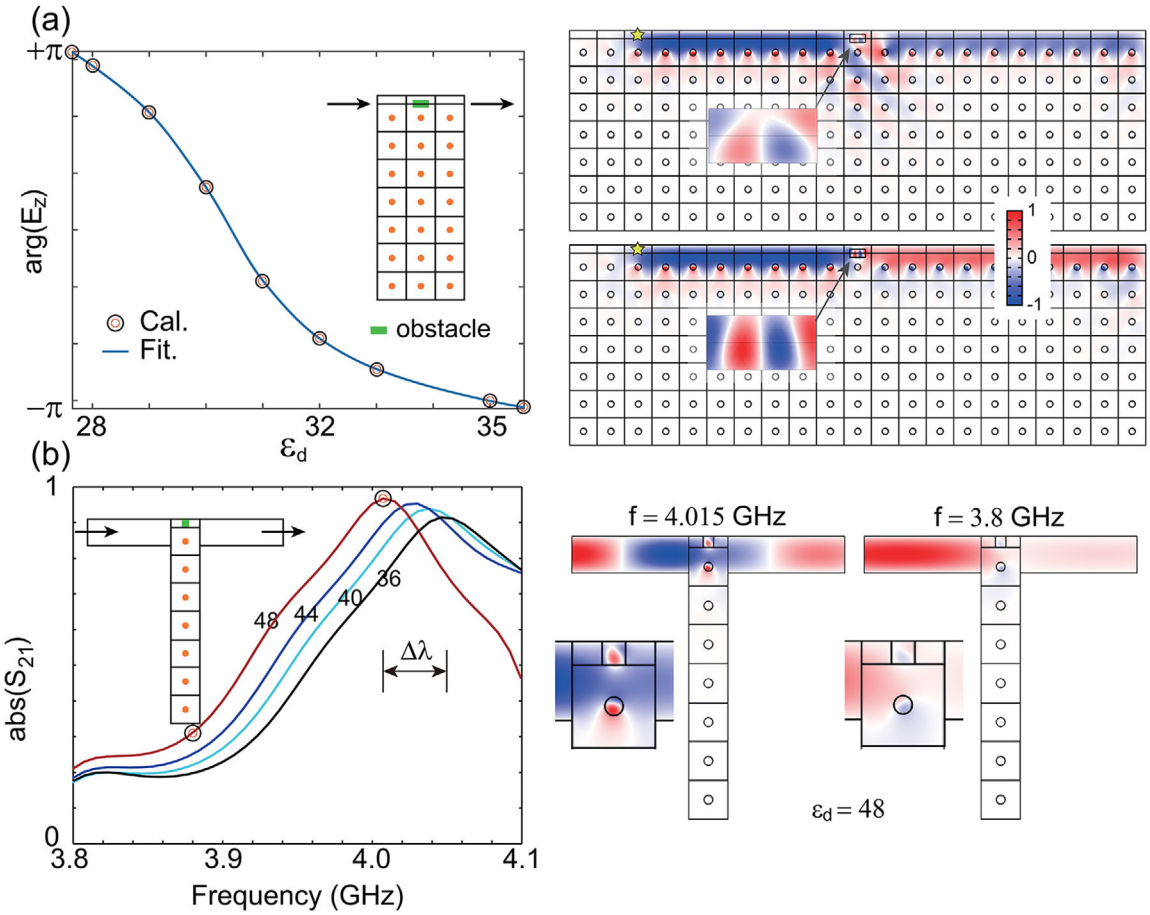


**Figure 9.** Two types of topological sensors. a) Phase angle of the output electric field as the permittivity of the obstacle changes from 27.65 to 35.6. The right panels show the electric-field distribution in the sensor for $\epsilon_d = 29$ (upper panel) and $\epsilon_d = 31$ (lower panel). Parameters: $f = f_0 = 3.85$ GHz, $\mu_1 \approx 8.43$, $\mu_2 \approx 6.81$, $a = 0.0418$ m, $d = 0.285a$, and $r = 0.11a$. b) Broadband topological sensing using one-way modes in PhCs. Four lines represent the total transmission performance for $\epsilon_d = 36$, 40, 44, and 48, respectively. The right two panels show simulations for different working frequencies, 3.8 GHz ($\mu_1 \approx 7.542$ and $\mu_2 \approx 5.919$) and 4.015 GHz ($\mu_1 \approx 14.774$ and $\mu_2 \approx 13.1669$), with $\epsilon_d = 48$, $a = 0.0418$ m, and $d = 0.285a$. The insets show the schematics of the two topological sensors.

bands by presetting the YIG frequency ($f_0$) and obtain the specific structural parameters of the INZ modes through iterative methods. Our calculations show that when an external magnetic field (e.g., 1500 G) is applied to the PhC, two nontrivial bandgaps appear, with inverse gap Chern numbers ($C_g = \pm 1$), implying the existence of one-way modes with opposite propagation directions in each band gap. Using iterative methods and FEM simulations, we show that the one-way INZ modes are tunable within a broad band by adjusting either the air thickness or the EMF, both of which are easily achievable in practice. Additionally, we verify these one-way INZ modes in 3D and time domains, demonstrating that the INZ modes in both nontrivial bandgaps are robust to backscattering. Identifying the type of one-way INZ modes in the Chern PhC is crucial, as different types lead to distinct light—matter interactions and applications.[48] Given their relatively high coupling efficiency with a traditional air-filled parallel-plate waveguide (not shown) and non-zero group velocity, the proposed INZ modes can be regarded as EMNZ-like. In our opinion, our proposed structures are one-way resonators, and such EMNZ-like modes refer to the lowest-order resonance. Exploring the in-depth physical origin of these INZ modes—though beyond the focus of this work—remains of significant interest and could be pursued using methods such as (boundary) effective medium theory.[49] A major challenge lies in the strong dispersion effects, particularly when the INZ frequency deviates significantly from the Dirac point.

Taking advantage of the robust one-way propagation and theoretical zero phase shift, INZ modes have potential for various all-optical functionalities. In this work, we propose three INZ-based applications: a phase inverter, a 50/50 splitter, and a topological sensor. For the phase inverter, we design a three-part structure with the air layer thickness in the middle section slightly larger than in the other INZ sections. A phase shift occurs at the head and tail of the middle section, enabling phase inversion for certain thickness parameters. For the 50/50 splitter, we design a cross structure consisting of two PhCs under a reversed EMF ($B_1 = -B_0$) and one air layer. We theoretically study the dispersion relation and identify an INZ mode in the odd-mode curves. Due to symmetry, the input wave in the bandgap is perfectly and equally divided into two channels (i.e., 50/50), with either the same or

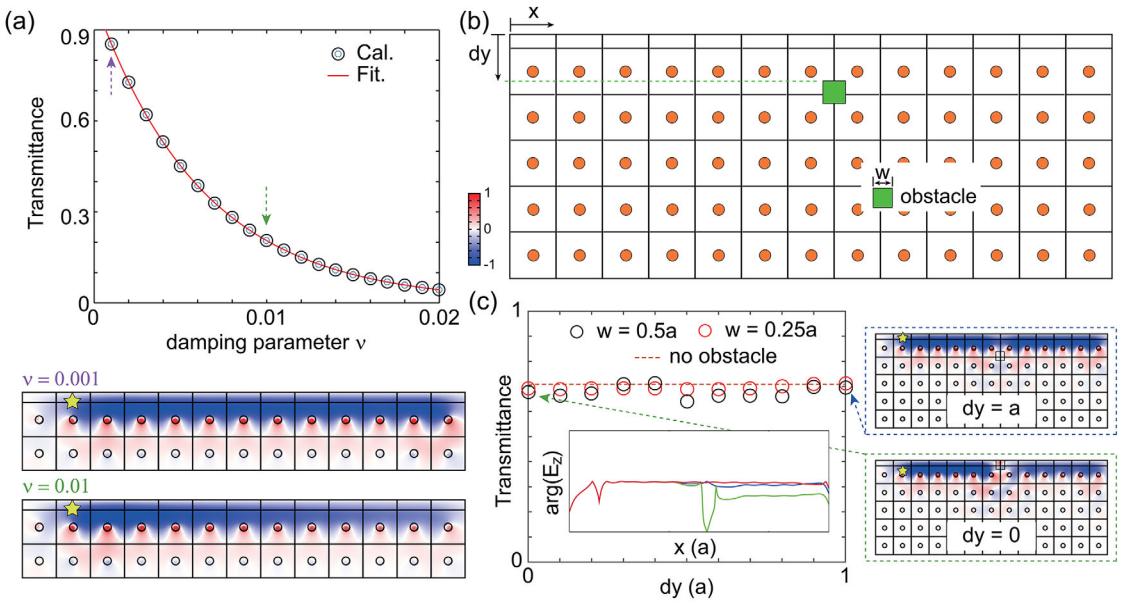


**Figure 10.** Verification of the robustness of one-way INZ modes. a) Transmittance of an INZ mode as a function of the damping parameter $\nu$. The lower panels show the $E_z$ distributions for $\nu = 0.001$ (first) and $\nu = 0.01$ (second). b) Schematic of a Chern PhC with a square silicon obstacle ($\epsilon_{si} = 11.68$) of side length $w$. The distance between the upper edge of the silicon and that of the Chern PhC is defined as $dy$. c) Transmittance of the same INZ mode as in (a), plotted as a function of $dy$. The black and red circles indicate different obstacle sizes. The horizontal dashed line marks the transmittance of the INZ mode for $w = 0$ (no obstacle). The inset shows the phase oscillation along the $x$ direction at the air—PhC interface for $w = 0$ (red), $w = 0.5a$ and $dy = a$ (blue), and $w = 0.5a$ and $dy = 0$ (green). $\nu = 0.001$ in (c). Other parameters are identical to those in Figure 9a.

reversed output phases. Additionally, two types of broadband, high-performance topological sensors are developed by comparing the output phase (first sensor) or the transmission (second sensor). The effects of loss on the INZ modes, as well as their robustness to disorders, are investigated and confirmed through parameter sweeps. Our findings suggest a new avenue for optical communication and computing, with potential for further applications in the field.

## Acknowledgements

J.X. and Y.L. contributed equally to this work. This work was supported by the National Natural Science Foundation of China (NSFC) (No. 12404143, No. 62101496), and the Program of Luzhou Science and Technology Bureau (No. 2023JYJ046, No. 2023JYJ032), the Sichuan Science and Technology Program (No. 2022YFS0616), and the General Secretariat for Research and Technology (GSRT) and the Hellenic Foundation for Research and Innovation (HFRI) under Grant No. 4509.

## Conflict of Interest

The authors declare no conflict of interest.

## Data Availability Statement

The data that support the findings of this study are available from the corresponding author upon reasonable request.

## Keywords

chern number, index-near-zero mode, sensors, topological photonic crystals

Received: April 10, 2025
Revised: May 30, 2025
Published online:

[1] K. V. Klitzing, G. Dorda, M. Pepper, *Phys. Rev. Lett.* **1980**, *45*, 494.
[2] K. L. Tsakmakidis, O. Hess, R. W. Boyd, X. Zhang, *Science* **2017**, *358*, eaan5196.
[3] J. F. Karcher, S. Gopalakrishnan, M. C. Rechtsman, *Phys. Rev. A* **2024**, *109*, 063507.
[4] K. L. Tsakmakidis, A. D. Boardman, O. Hess, *Nature* **2007**, *450*, 397.
[5] F.-F. Li, H.-X. Wang, Z. Xiong, Q. Lou, P. Chen, R.-X. Wu, Y. Poo, J.-H. Jiang, S. John, *Nat. Commun.* **2018**, *9*, 2462.
[6] M. Jamali, J. H. Kwon, S.-M. Seo, K.-J. Lee, H. Yang, *Sci. Rep.* **2013**, *3*, 3160.
[7] J. Xu, F. Kang, Y. Luo, S. Xiao, K. L. Tsakmakidis, *Adv. Opt. Mater.* **2023**, *11*, 2201836.
[8] P. Pintus, M. Dumont, V. Shah, T. Murai, Y. Shoji, D. Huang, G. Moody, J. E. Bowers, N. Youngblood, *Nat. Photonics* **2025**, *19*, 54.
[9] Z. Wang, Y. Chong, J. D. Joannopoulos, M. Soljačić, *Phys. Rev. Lett.* **2008**, *100*, 013905.
[10] Z. Wang, Y. Chong, J. D. Joannopoulos, M. Soljačić, *Nature* **2009**, *461*, 772.
[11] Y. Ding, Y. Peng, Y. Zhu, X. Fan, J. Yang, B. Liang, X. Zhu, X. Wan, J. Cheng, *Phys. Rev. Lett.* **2019**, *122*, 014302.
[12] L. He, Z. Addison, J. Jin, E. J. Mele, S. G. Johnson, B. Zhen, *Nat. Commun.* **2019**, *10*, 4194.
[13] S. A. H. Gangaraj, F. Monticone, *Phys. Rev. Lett.* **2020**, *124*, 153901.
[14] Y. Hatsugai, *Phys. Rev. Lett.* **1993**, *71*, 3697.
[15] N. Regnault, B. A. Bernevig, *Phys. Rev. X* **2011**, *1*, 021014.
[16] E. M. Spanton, A. A. Zibrov, H. Zhou, T. Taniguchi, K. Watanabe, M. P. Zaletel, A. F. Young, *Science* **2018**, *360*, 62.

[17] X. Xi, K.-P. Ye, R.-X. Wu, *Photonics Res.* **2020**, *8*, B1.
[18] J.-W. Dong, X.-D. Chen, H. Zhu, Y. Wang, X. Zhang, *Nat. Mater.* **2017**, *16*, 298.
[19] B. Yan, Y. Peng, J. Xie, Y. Peng, A. Shi, H. Li, F. Gao, P. Peng, J. Jiang, J. Liu, F. Gao, S. Wen, *Laser Photonics Rev.* **2024**, *18*, 2300686.
[20] H. Xue, Y. Yang, B. Zhang, *Nat. Rev. Mater.* **2022**, *7*, 974.
[21] G.-G. Liu, Z. Gao, Q. Wang, X. Xi, Y.-H. Hu, M. Wang, C. Liu, X. Lin, L. Deng, S. A. Yang, P. Zhou, Y. Yang, Y. Chong, B. Zhang, *Nature* **2022**, *609*, 925.
[22] G. E. Lio, A. Ferraro, B. Zappone, J. Parka, E. Schab-Balcerzak, C. P. Umeton, F. Riboli, R. Kowerdziej, R. Caputo, *Adv. Opt. Mater.* **2024**, *12*, 2302483.
[23] A. Pianelli, V. Caligiuri, M. Dudek, R. Kowerdziej, U. Chodorow, K. Sielezin, A. De Luca, R. Caputo, J. Parka, *Sci. Rep.* **2022**, *12*, 16961.
[24] R. Kowerdziej, A. Ferraro, D. C. Zografopoulos, R. Caputo, *Adv. Opt. Mater.* **2022**, *10*, 2200750.
[25] K. Sun, C. Wang, J. Tian, Z. Zhang, N. Zeng, R. Yin, W. Duan, Q. Hou, Y. Zhao, H. Wu, R. Fan, *Adv. Funct. Mater.* **2024**, *34*, 2306747.
[26] J. B. Pendry, *Phys. Rev. Lett.* **2000**, *85*, 3966.
[27] D. R. Smith, J. B. Pendry, M. C. Wiltshire, *Science* **2004**, *305*, 788.
[28] I. Liberal, N. Engheta, *Nat. Photonics* **2017**, *11*, 149.
[29] L. Caspani, R. Kaipurath, M. Clerici, M. Ferrera, T. Roger, J. Kim, N. Kinsey, M. Pietrzyk, A. Di Falco, V. M. Shalaev, A. Boltasseva, D. Faccio, *Phys. Rev. Lett.* **2016**, *116*, 233901.
[30] O. Reshef, I. De Leon, M. Z. Alam, R. W. Boyd, *Nat. Rev. Mater.* **2019**, *4*, 535.
[31] D. Bi, Z. Guo, Q. Wang, Q. Wei, J. Wu, Y. Sun, Y. Chen, Y. Yang, H. Jiang, H. Chen, *Laser Photonics Rev.* **2025**, *19*, 2401900.
[32] X. Huang, Y. Lai, Z. H. Hang, H. Zheng, C. T. Chan, *Nat. Mater.* **2011**, *10*, 582.
[33] Y. Li, C. T. Chan, E. Mazur, *Light: Sci. Appl.* **2021**, *10*, 203.
[34] C. Xu, G. Ma, Z.-G. Chen, J. Luo, J. Shi, Y. Lai, Y. Wu, *Phys. Rev. Lett.* **2020**, *124*, 074501.
[35] M. H. Javani, M. I. Stockman, *Phys. Rev. Lett.* **2016**, *117*, 107404.
[36] N. Kinsey, C. DeVault, A. Boltasseva, V. M. Shalaev, *Nat. Rev. Mater.* **2019**, *4*, 742.
[37] D. I. Vulis, O. Reshef, P. Camayd-Muñoz, E. Mazur, *Rep. Prog. Phys.* **2019**, *82*, 012001.
[38] S. A. Skirlo, L. Lu, Y. Igarashi, Q. Yan, J. Joannopoulos, M. Soljačić, *Phys. Rev. Lett.* **2015**, *115*, 253901.
[39] D. Xiao, M.-C. Chang, Q. Niu, *Rev. Mod. Phys.* **2010**, *82*, 1959.
[40] T. Fukui, Y. Hatsugai, H. Suzuki, *J. Phys. Soc. Jpn.* **2005**, *74*, 1674.
[41] R.-Y. Zhang, X. Cui, Y.-S. Zeng, J. Chen, W. Liu, M. Wang, D. Wang, Z.-Q. Zhang, N. Wang, G.-B. Wu, C. T. Chan, *Nature* **2025**, *641*, 1142.
[42] W. Tong, J. Wang, J. Wang, Z. Liu, Y. Pang, S. Qu, *Appl. Phys. Lett.* **2016**, *109*, 053502.
[43] A. Tittl, H. Giessen, N. Liu, *Nanophotonics* **2014**, *3*, 157.
[44] H. Zhao, T. Zhang, X. Zhang, M.-H. Lu, Y.-F. Chen, *Front. Phys.* **2022**, *10*, 844417.
[45] R. Fleury, D. L. Sounas, C. F. Sieck, M. R. Haberman, A. Alù, *Science* **2014**, *343*, 516.
[46] X.-F. Li, X. Ni, L. Feng, M.-H. Lu, C. He, Y.-F. Chen, *Phys. Rev. Lett.* **2011**, *106*, 084301.
[47] C. Lu, X. Hu, Y. Zhang, Z. Li, X. Xu, H. Yang, Q. Gong, *Appl. Phys. Lett.* **2011**, *99*, 051107.
[48] Z. Guo, H. Jiang, H. Chen, *J. Phys. D: Appl. Phys.* **2022**, *55*, 083001.
[49] N. Wang, R.-Y. Zhang, C. T. Chan, G. P. Wang, *Phys. Rev. B* **2020**, *102*, 094312.

 